J. Fluid Mech. (1995), *vol.* 285, *pp.* 303–327

The primary and inverse instabilities of directional viscous fingering

By D. A. REINELT

Department of Mathematics, Southern Methodist University, Dallas, TX 75275, USA

(Received 8 November 1993 and in revised form 12 September 1994)

Consider two infinitely long cylinders of different radii with one inside the other but off-centred. The gap between the two cylinders is partially filled with a viscous fluid. As the cylinders rotate with independent velocities U_1 and U_2, a thin liquid film coats each of their surfaces all the way around except in the region where the viscous fluid completely fills the gap. Interface conditions that connect solutions of averaged equations in the viscous fluid region with solutions in the thin film region are derived. For the two-interface problem analysed here, two types of instabilities occur depending on the amount of viscous fluid between the cylinders. For large fluid volume, the primary supercritical instability occurs when the front interface becomes unstable as the cylinder velocities are increased. For small fluid volume, the back interface passes through the region where the gap width is a minimum to the same side as the front interface. Steady state solutions with straight interface edges exhibit a turning point with respect to the cylinder velocities. The back interface becomes unstable at the turning point; this inverse instability is subcritical.

1. Introduction

In recent years, new experiments have been performed that re-examine coating flows originally analysed by Pearson (1960) and Pitts & Greiller (1961). These experiments have been carried out with a number of different geometries: half-submerged counter-rotating cylinders located next to each other (Coyle, Macosko & Scriven 1990), a rotating cylinder and a flat plate (Hakim *et al.* 1990) and non-concentric co-rotating or counter-rotating cylinders as shown in figure 1 (Rabaud, Michalland & Couder 1990; Rabaud & Hakim 1991; Michalland 1992; Pan & de Bruyn 1993).

There have been a number of different mathematical models developed for the coating flow problems listed above. The objective of these models is to determine the position and stability of an interface edge as a function of cylinder velocity. In figure 1, the two interface edges correspond to the points at the tip of the tongue-shaped interfaces; the actual interface edges come out of the page. In a typical coating flow problem, the interface edge is initially straight for small cylinder velocities. As the cylinder velocities increase, the edge becomes unstable and takes on a sinusoidal shape. For larger velocities the interface edge is composed of deep cells or viscous fingers. This instability is commonly referred to as the 'ribbing' instability.

We observe that when the cylinders in figure 1 are rotating with equal velocities ($U_1 = U_2$) the interface edge moving in the reference frame of the boundaries is similar to an interface edge moving in a Hele-Shaw cell. It is known that when a less viscous fluid forces a more viscous fluid from the gap between parallel plates

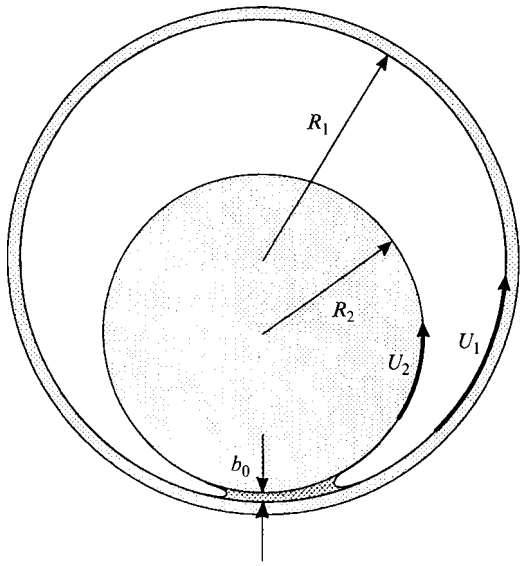

FIGURE 1. Sketch of the rotating cylinders and the two menisci. The cylinders with radii R_1 and R_2 rotate with velocities U_1 and U_2. The minimum gap width between the two cylinders is b_0.

(Hele-Shaw cell) in a direction perpendicular to the interface that the interface is unstable to small disturbances (Saffman & Taylor 1958). The opposite case is stable. This means that if the cylinders are moving in the direction shown in the figure this same instability mechanism tends to make the interface edge on the right unstable and the one on the left stable.

In contrast to the flow between parallel plates where the gap width is constant, the above coating flow problems all have a variable gap width. This varying gap width adds a stabilizing factor due to the pressure jump across the interface. To leading order (small velocities) the pressure jump is given by $p_0 - p \sim \Delta p \sim 2T/b$, where p_0 is the constant pressure of the air, p is fluid pressure, T is surface tension, and b is the gap width at the interface edge. For a wavy interface, smaller b corresponds to lower fluid pressure at the interface; thus, the effect of a varying gap width is fluid motion along the interface from large-b to small-b regions which decreases the amplitude of a disturbance on the interface. These competing effects mean that unlike the Hele-Shaw problem where the interface is always unstable, there is a finite value of velocity at which the instability first occurs.

Rabaud *et al.* (1990) have done an experimental study of the different dynamical regimes that occur for the apparatus shown in figure 1 for both co-rotating and counter-rotating cylinders. Their stability diagram is shown in figure 2. Depending on the choice of the cylinder velocities U_1 and U_2, they observe stationary periodic cells, solitary waves that travel on top of these cells, and cells that travel into the page or out of the page (see figure 1). In addition, for some values of the velocities, they observe strong fluctuations in wavelength and constant formation and destruction of cells. They refer to this behaviour as 'spatiotemporal chaos'. One of the objectives of this research is to develop equations that will allow us to study some of these different types of phenomena.

Most mathematical models for the coating flow problems discussed above assume that the lubrication approximation can be used to describe the flow of the viscous

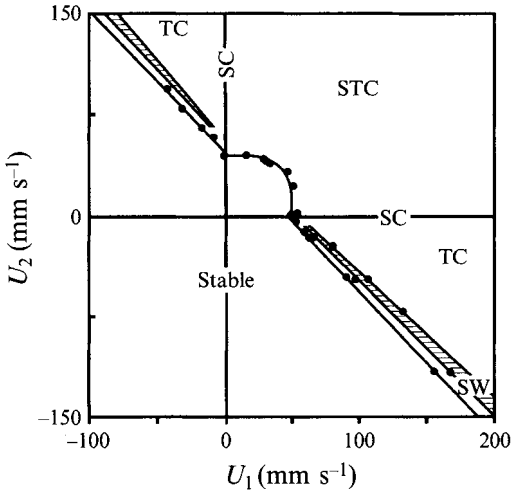

FIGURE 2. Stability diagram for the experimental results of Rabaud *et al.* (1990). Results correspond to $b_0/R_2 = 7.55 \times 10^{-3}$. They observed stationary periodic cells (SC), travelling cells (TC), solitary waves (SW) moving on a stationary sinusoidal front, and spatiotemperal chaos (STC). Reprinted with permission.

fluid in the narrow region between the cylinders and away from the menisci or interface edges. This approximation leads to equations for the velocity components that have been averaged across the gap and for a pressure that is independent of the direction across the gap. This means that two-dimensional flow corresponding to straight interface edges is replaced by a one-dimensional problem and that three-dimensional flow corresponding to interface edges with lateral variations is replaced by a two-dimensional problem.

The major difficulty with the above approach is finding appropriate boundary conditions that connect the averaged equations valid in the viscous fluid region with equations that describe the thin liquid films that coat the cylinders. The averaged equations derived from the lubrication approximation are not valid in the neighbourhood of a meniscus. As we approach the meniscus, the flow becomes two-dimensional when we have straight interface edges and three-dimensional when the edges have lateral variations. The boundary conditions should be derived from the fluid flow in the meniscus region.

Another approach that can be used when the interface edges are straight is to solve the full two-dimensional problem directly. This was done by Coyle, Macosko & Scriven (1986) for partially submerged forward roll coating. If the ultimate objective is to determine interface edge shapes with lateral variations, then reducing the three-dimensional problem to a two-dimensional problem using the averaged equations and appropriate boundary conditions is a promising approach; solving the full three-dimensional problem directly involves very intensive computations.

Many different variations on the boundary conditions have been used; some of these conditions have been reviewed by Savage (1977). In recent years, approximations to the pressure jump boundary condition have taken the form

$$\Delta p = \frac{T}{b_0}\left[F_0 + \frac{b_0}{R}F_1 + \frac{\mathrm{d}b}{\mathrm{d}x}F_2 + \cdots\right], \tag{1.1}$$

where R is the radius of curvature in the lateral direction (along the interface edge)

and db/dx gives the linear divergence of the cylinders in the meniscus region. F_i are functions of the capillary numbers, $Ca_1 = \mu U_1/T$ and $Ca_2 = \mu U_2/T$, where μ is the fluid viscosity. The capillary number gives the ratio of viscous forces to the force of surface tension. To get the leading-order contribution to the pressure jump (F_0) for $Ca_1 = Ca_2$, the cylinders in the meniscus region are approximated by parallel plates (the Hele-Shaw cell problem). This problem has been solved for small capillary numbers by Bretherton (1961) using perturbation methods and solved for finite capillary numbers by Ruschak (1982) using numerical methods.

To get the next-order corrections to the boundary conditions, one must account for variations along the interface edge and the linear divergence of the cylinders in the meniscus region. Here, we assume that the minimum gap width b_0 divided by an appropriate length scale along the interface edge is a small quantity and the same order of magnitude as the derivative of gap width with respect to distance along the cylinder.

Park & Homsy (1984) used perturbation methods to determine the small capillary number correction to the boundary conditions that accounts for lateral variations of the interface edge. Reinelt (1987) solved this problem numerically for finite capillary numbers. In both cases, the solution was determined between parallel plates. These results are valid in the meniscus region for the coating flow problems discussed here. Corrections to the boundary conditions due to the linear divergence of the cylinders in the meniscus region have not been determined. The coupling of a diverging gap width and lateral edge variations is a higher-order effect that is not needed.

The above approaches all assume that in the reference frame of the tip of the meniscus both cylinders or parallel plates have equal velocities. To study the different regimes shown in figure 2, boundary conditions that account for different cylinder velocities need to be determined. In addition, when the cylinder velocities are positive as shown in figure 1, these boundary conditions are only valid for the right-hand interface edge and not the left-hand interface edge.

At the right-hand meniscus, the thickness of each thin film is determined as part of the solution. Once the thin films have been pulled out of the viscous fluid, they are then carried around to the left-hand meniscus by the cylinders and pushed back into the viscous fluid. We note that for a wavy interface edge, the thin films that coat the cylinders have variable thickness in the direction parallel to the cylinder axes. In this analysis, we assume that changes in film thickness due to levelling in the direction of the cylinder axes or gravity occur on a time scale that is much longer than the time it takes the cylinder to complete one revolution. Using this assumption, the appropriate boundary conditions at the left meniscus will be a function of the capillary numbers and a function of film thickness as determined at the right interface.

In the past, it has been assumed that the left interface in the two interface problem is far enough away from the right interface that it can be ignored in calculating the position and stability of the right interface. In figure 2, many of the interesting phenomena occurs for counter-rotating cylinders. In this case, each interface edge has one thin film that is being pulled out of the viscous fluid and another being pushed back into the viscous fluid; thus, it is definitely necessary to account for both interfaces in the counter-rotating problem.

In this research, we determine steady state solutions for both co-rotating and counter-rotating cylinders and analyse their stability. We refer to this instability as the 'primary' instability. A second kind of instability has been found when the amount of fluid placed in the apparatus is small. When both cylinders are rotating in the same direction as shown in figure 1, the left interface moves to the right of the

position where the gap width is a minimum. When this occurs, the effect of a varying gap width on the left interface is now destabilizing. Note that the fluid and air have switched places relative to the direction in which the gap narrows. This means that at the left interface, there are now competing effects: the more viscous fluid pushing out the less viscous fluid (relative to the motion of the cylinders) is stabilizing and the varying gap width is destabilizing. These competing effects are directly opposite to those effects still competing at the right interface.

As the velocities of the cylinders increase, the left interface becomes unstable before the right interface. We refer to this instability as the 'inverse' instability. This new instability has recently been observed in experiments by Michalland (1992). It is not possible to get this instability without a mathematical model that accounts for both interfaces. Results for both the primary and inverse instabilities are discussed below.

2. Derivation of equations

2.1. *Local coordinate system*

In the coating flow problem shown in figure 1, we assume that the minimum gap width b_0 is much smaller than R_2, the radius of the small cylinder. The ratio R_2/R_1 is an $O(1)$ quantity, but the equations derived below are also valid for a cylinder and a flat plate if one sets $U_1 = 0$ and lets $R_1 \to \infty$. In addition, the equations are valid for both co-rotating and counter-rotating cylinders. The effect of gravity on the solutions is neglected.

To find an expression for the gap width b in terms of position along the outer cylinder, we introduce a cylindrical coordinate system (r, ϕ, y) at the centre of the large cylinder, where $\phi = 0$ corresponds to $b = b_0$ and the y-coordinate is parallel to the axes of the cylinders. By neglecting terms of $O(b_0/R_2)$ and by assuming that the volume of liquid is small enough so that b/b_0 is an $O(1)$ quantity in the region between the two menisci, we get the following approximation for the gap width:

$$\frac{b(x)}{b_0} = 1 + \frac{1}{2}\left(1 - \frac{R_2}{R_1}\right)\frac{R_1^2\phi^2}{R_2 b_0} = 1 + \frac{x^2}{a_0^2}\,. \tag{2.1}$$

Here, $x = R_1\phi$ is the physical variable along the large cylinder; thus, the gap width is measured along a line segment perpendicular to the outer cylinder. The length a_0 defined in (2.1) is given by

$$a_0 = (2R_2 b_0)^{1/2}\left(1 - \frac{R_2}{R_1}\right)^{-1/2}\,. \tag{2.2}$$

We define the quantity $\delta = b_0/a_0$ and note that $\delta = O((b_0/R_2)^{1/2}) \ll 1$. Throughout this analysis, we retain terms of $O(\delta)$ but neglect terms of $O(\delta^2) = O(b_0/R_2)$. We note that if R_2 is close to R_1, then δ is even smaller than the order given above.

Figures 3(*a*) and 3(*b*) show the top and side views of the region near where the gap width is smallest. The origin of the local coordinate system (x, y, z) is located at $(r, \phi, y) = (R_1, 0, 0)$; the z-coordinate is related to r by $z = R_1 - r$. The positions of the tip or leading edge of the left and right menisci are $x = x_L(y, t)$ and $x = x_R(y, t)$ as shown.

The dashed lines in figure 3(*a*) divide the physical domain into a centre region where the viscous fluid completely fills the gap, a thin film region on the far left and right that is connected by the moving cylinders, and a narrow region about each meniscus. Equations valid in the centre region (away from the menisci) are derived by

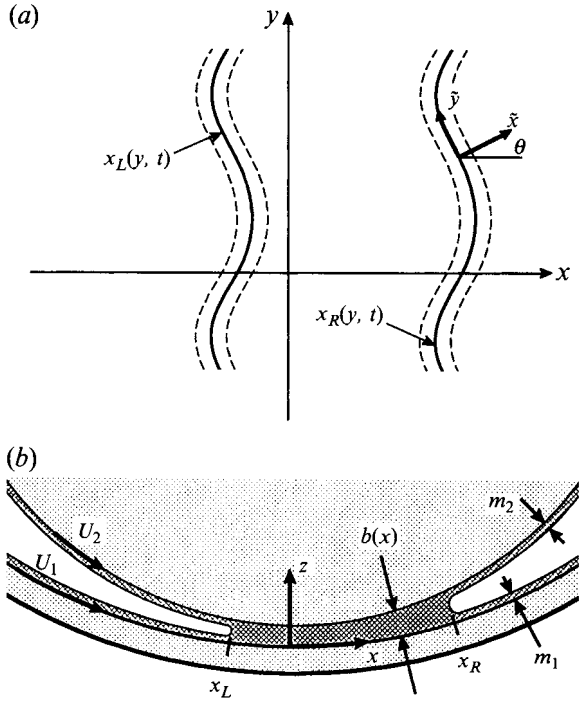

FIGURE 3. Viscous fluid region located between the tips of the two menisci located at $x_L(y,t)$ and $x_R(y,t)$. (*a*) Top view. The dashed lines indicate the meniscus region, where the averaged equations are no longer valid. The coordinate axes $\tilde{x}$ and $\tilde{y}$ move with the interface edge as shown. (*b*) Side view. Thin liquid films of thickness m_1 and m_2 coat the rotating cylinders. The variable gap width is $b(x)$.

averaging solutions of Stokes equations across the gap between the cylinders. Interface conditions that connect the solutions of these averaged equations with solutions in the thin film region are derived from local solutions valid in the neighbourhood of each meniscus.

2.2. *Averaged equations*

To derive the averaged equations valid in the centre region away from the menisci, we begin with Stokes equations written in the cylindrical coordinate system (r, ϕ, y) and convert these equations to the local coordinate system (x, y, z) using the change of variables discussed above. In the centre region, the appropriate length scale in the x- and y-directions is a_0, while the length scale in the z-direction is b_0. Neglecting terms of $O(\delta^2) = O(b_0/R_2)$, we get the usual lubrication approximation of Stokes equations:

$$\frac{\partial p}{\partial x} = \mu \frac{\partial^2 u}{\partial z^2}, \qquad \frac{\partial p}{\partial y} = \mu \frac{\partial^2 v}{\partial z^2}, \qquad \frac{\partial p}{\partial z} = 0; \tag{2.3}$$

$$\frac{\partial u}{\partial x} + \frac{\partial v}{\partial y} + \frac{\partial w}{\partial z} = 0\,. \tag{2.4}$$

The no-slip boundary condition at $z = 0$ is $(u, v, w) = (U_1, 0, 0)$; at $z = b(x)$, where $b(x)$ is given in (2.1), $(u, v, w) = (U_2, 0, (\mathrm{d}b/\mathrm{d}x)U_2)$. Here, $\mathrm{d}b/\mathrm{d}x$ is $O(\delta)$ and is retained.

Solving these equations subject to the boundary conditions, we get $p = p(x, y)$ and

$$u = U_1 + (U_2 - U_1)\frac{z}{b(x)} + \frac{z(z - b(x))}{2\mu}\frac{\partial p}{\partial x}, \qquad v = \frac{z(z - b(x))}{2\mu}\frac{\partial p}{\partial y}.$$

The velocity component in the z-direction is not given here, but is easily derived from (2.4) and the boundary conditions. By integrating the velocity components and the mass conservation equation from $z = 0$ to $z = b(x)$ and dividing by $b(x)$, we get the averaged velocity components,

$$\bar{u} = -\frac{b^2}{12\mu}\frac{\partial p}{\partial x} + \frac{1}{2}(U_1 + U_2), \qquad \bar{v} = -\frac{b^2}{12\mu}\frac{\partial p}{\partial y}, \tag{2.5}$$

and the corresponding averaged continuity equation,

$$\frac{\partial(b\bar{u})}{\partial x} + \frac{\partial(b\bar{v})}{\partial y} = 0. \tag{2.6}$$

2.3. *Interface conditions*

Before solving the averaged equations given in (2.5) and (2.6), it is necessary to derive interface conditions that connect the region where the averaged equations are valid with the region where the thin films are located. They are derived from local solutions valid in the neighbourhood of each meniscus. To determine these local solutions, we introduce the edge coordinate system shown in figure 3(*a*). The coordinates $\tilde{x}$ and $\tilde{y}$ vary in the directions perpendicular and tangential to the interface with $\tilde{x} = 0$ at the tip or edge of the meniscus; thus, the coordinate system moves with the interface. The variable θ is the angle between the x- and $\tilde{x}$-axes.

Figure 4(*a*) shows a side view of the region near the right meniscus with the tip of the tongue-shaped interface located at $x = x_R(y, t)$. This $(\tilde{x}, z)$-planar cross-section is perpendicular to the interface edge. The velocity components of the cylinders in the $\tilde{x}$-direction are $U_1 \cos\theta_R$ and $U_2 \cos\theta_R$ as shown. U_{nR} is the component of the interface edge velocity in the same direction.

If the equations are expressed in terms of the dimensionless variables appropriate for the viscous fluid region, then the width of the meniscus region is $O(\delta)$. We replace this narrow region in which a given quantity changes rapidly from one value to another by a discontinuity in that quantity and an appropriate jump condition. These jump conditions are analogous to shock conditions in gas-dynamics or other fluid dynamics problems. In deriving these conditions, it is helpful to view the meniscus region as vanishingly small as shown in figure 4(*b*). In this context, it is understood that the solution in the meniscus region provides the smooth transition between the viscous fluid solution in the limit as we approach the interface edge and the solution in the thin film region.

There are two interface conditions. The kinematic condition or conservation of fluid at the interface edge is given by

$$b(x_j)\bar{u}_{nj} = m_1 U_1 \cos\theta_j + m_2 U_2 \cos\theta_j + U_{nj}[b(x_j) - m_1 - m_2], \tag{2.7}$$

where $j = L, R$ refers to the left and right meniscus, $\bar{u}_{nj} = \bar{u}_j \cos\theta_j + \bar{v}_j \sin\theta_j$ is the averaged velocity normal to the interface edge, m_1 and m_2 give the thickness of the thin film on the larger and smaller cylinders, and $U_{nj} = (\partial x_j/\partial t)\cos\theta_j$ is the normal velocity of the interface edge. In words, the amount of fluid flowing out of the region where the averaged equations are valid must equal the amount of fluid flowing into the two thin films plus the flow due to the moving interface. The effect on the

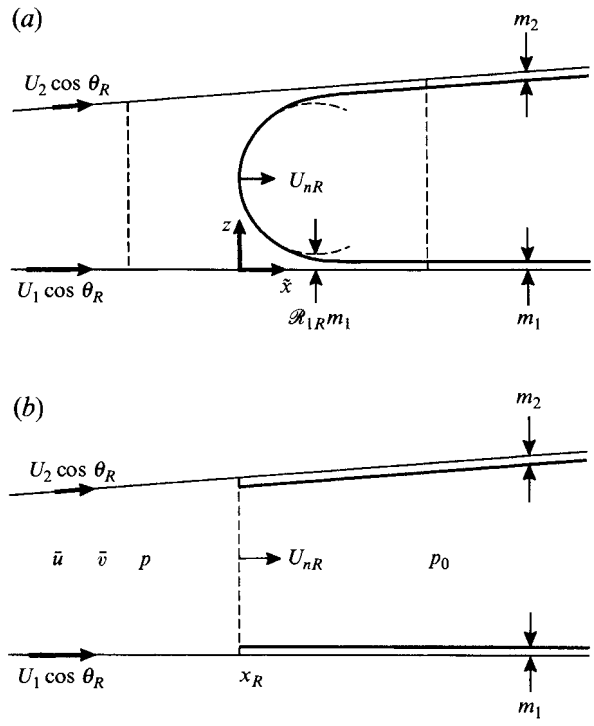

FIGURE 4. Region near the right meniscus. (*a*) Side view showing the $(\tilde{x}, z)$-plane which is perpendicular to the interface edge $x_R(y, t)$. (*b*) Side view in the limit in which the meniscus region vanishes.

kinematic condition from fluid flow parallel to the interface edge is neglected. The pressure jump condition at $x = x_L$ and $x = x_R$ is expressed as

$$p_0 - p(x_j) = \Delta p_j \,, \tag{2.8}$$

where p_0 is the pressure of the air and the fluid in the thin films and p is the pressure in the region where the averaged equations are valid.

To complete the formulation of the problem, we require that the total amount of fluid be conserved. If V_0 is the volume of fluid located between $y = y_1$ and $y = y_2$, then

$$V_0 = \int_{y_1}^{y_2} \left[\int_{x_L}^{x_R} b(x)\mathrm{d}x + (2\pi R_1 - \Delta x)m_1 + (2\pi R_2 - \Delta x)m_2 + A_L + A_R \right] \mathrm{d}y \,, \tag{2.9}$$

where $b(x)$ given in (2.1) is easily integrated from x_L to x_R and $\Delta x = x_R - x_L$. The first term is the volume of fluid between the tips of the two menisci, the second and third terms give the volume of fluid in the two thin films, and the last two terms are the remaining fluid near the two menisci not accounted for by the other terms; thus, A_L and A_R give the cross-sectional area of the region between x_L and the left meniscus and x_R and the right meniscus.

The functions m_1, m_2, Δp_j, A_L and A_R are determined from solutions of the appropriate two-dimensional Stokes equations in the the plane perpendicular to the interface edge ($\tilde{y}$ = constant) or $(\tilde{x}, z)$-plane as shown in figure 4(*a*). These equations are derived by changing from the (x, y, z) to the $(\tilde{x}, \tilde{y}, z)$ coordinate system and then scaling the variables appropriately. Near the meniscus, the appropriate lengthscale

in the $\tilde{x}$- and z-directions is b_0 and the lengthscale in the $\tilde{y}$-direction is a_0. A more detailed analysis of this problem for a Hele-Shaw cell corresponding to $b(x) = b_0$ and $U_1 = U_2$ can be found in Reinelt (1987). Solutions are determined using perturbation methods for small capillary numbers or using numerical methods for $O(1)$ capillary numbers.

2.4. *Interface conditions: perturbation results*

Assuming that the capillary numbers are small, we derive results similar to the interface conditions derived by Park & Homsy (1984) for two-phase displacement in a Hele-Shaw cell. The major differences between their results and those discussed here are that we account for a gap width that varies with x, two different velocities on the walls of the cylinders, and thin films that are pulled out of and pushed into the region where the viscous fluid fills the gap.

In the limit as the capillary numbers tend to zero, the thickness of the thin films m_1 and m_2 is zero and the jump in pressure is balanced by the effective pressure due to surface tension and the curvature of the interface. In the plane perpendicular to the interface edge, the static meniscus is just an arc of a circle with radius of curvature ρ_j (figure 4*a* shows the arc of the circle for the case when m_1 and m_2 are not zero). Along the interface edge $x = x_j(y,t)$, the curvature $C_j(y,t)$ is given by

$$C_j = \frac{\partial^2 x_j/\partial y^2}{\left[1 + \left(\partial x_j/\partial y\right)^2\right]^{3/2}} . \tag{2.10}$$

We note that the curvature varies with position along the interface edge and is not known until the averaged equations are solved and the shape of the interface edges are determined.

In terms of the above quantities, the jump in pressure across the static meniscus at the right interface is

$$\Delta p_R = \frac{T}{\rho_R} + \frac{\pi}{4} T C_R . \tag{2.11}$$

This form of the pressure jump is only valid if $1/\rho_R$, the curvature across the gap, is much larger than C_R, the curvature along the interface edge. The radius ρ_R is chosen so that the interface approaches the cylinders tangentially. To leading order, it is just equal to half of the gap width at the tip of the meniscus; thus, $\rho_R \sim \rho_0 = b(x_R)/2$. We have assumed that the appropriate lengthscale along the interface edge is a_0 so that the curvature C_R is $O(1/a_0)$; thus, the second curvature term in (2.11) is $O(\delta)$ smaller than the first term. Without this assumption, it would be necessary to solve the full three-dimensional Stokes equations. The factor $\pi/4$ in front of the second term arises in solving the $O(\delta)$ curvature equation and in choosing the unknown constants such that the interface approaches the cylinders tangentially (see Park & Homsy 1984; Reinelt 1987).

To find the $O(\delta)$ correction to the radius of the static meniscus ρ_R, we note that the gap is wider at the position where the meniscus meets the cylinders tangentially than it is at the tip. The points where the meniscus and cylinders meet correspond to $\tilde{x} = \tilde{x}_0 = b(x_R)/2$ or the value of x given within the brackets below; thus, the diameter of the static meniscus is

$$2\rho_R \sim b\left[x_R + \frac{b(x_R)}{2}\cos\theta_R\right] \sim b(x_R) + \frac{b}{2}\frac{\mathrm{d}b}{\mathrm{d}x}\cos\theta_R . \tag{2.12}$$

For the local coordinate system defined above, the $\tilde{x}$ value at which the interface

intersects the upper cylinder is slightly smaller than the $\tilde{x}$ value at which the interface intersects the lower cylinder. This difference leads to a term that is $O(b_0\delta^2)$; terms of this magnitude are neglected throughout this analysis.

We now derive the leading-order dependence of m_1, m_2 and Δp on small capillary number. As discussed by Bretherton (1961) in his analysis of the motion of long bubbles in tubes, the leading-order effect of small capillary number enters the problem at $O(Ca^{2/3})$. Neglecting terms of $O(Ca)$, there is still a static meniscus in the plane perpendicular to the interface edge that is valid away from the region where the meniscus meets the cylinders; thus, the pressure jump given in (2.11) is still valid except that $2\rho_R$ (the diameter of the dashed circle shown in figure 4*a*) is now given by

$$2\rho_R \sim b(x_R) + \frac{b}{2}\frac{\mathrm{d}b}{\mathrm{d}x}\cos\theta_R - m_1\mathscr{R}_1 - m_2\mathscr{R}_2 . \tag{2.13}$$

The last two terms account for the presence of the thin films of thickness m_1 and m_2; $\mathscr{R}_1$ and $\mathscr{R}_2$ are numerical constants that need to be determined. One might guess that we could simply set $\mathscr{R}_1 = \mathscr{R}_2 = 1$ so that a meniscus or arc of a circle with radius ρ_R would meet up with the two thin films of constant thickness m_1 and m_2. Unfortunately, the problem is not this simple; there is a transition region in the vicinity of the ends of the meniscus at $\tilde{x} = \tilde{x}_0$ where some of the $O(Ca)$ terms in the Stokes equations valid in the $(\tilde{x}, z)$-plane can no longer be neglected. New equations are derived by introducing a new set of scalings in the transition region (Park & Homsy 1984; Reinelt 1987).

In the transition region located near the point $\tilde{x} = \tilde{x}_0$ and $z = 0$ on the larger cylinder, solutions of these new equations lead to the following ordinary differential equation for film thickness $m(\tilde{x})$:

$$\frac{\mathrm{d}^3 m}{\mathrm{d}\tilde{x}^3} = -3Ca_1\cos\theta_R\frac{m - m_1}{m^3} . \tag{2.14}$$

This equation arises in coating flows (Landau & Levich 1942), withdrawal of soap films from Plateau borders (Mysels, Shinoda & Frankel 1959), long bubble in tubes (Bretherton 1961), etc. The correct solution of this ordinary differential equation must asymptote to the constant film thickness m_1 as $\tilde{x} \to \infty$ and must also match onto the asymptotic expansion of the equation that describes the static meniscus. The asymptotic expansion of the static meniscus of radius ρ_R as it approaches the transition region ($\tilde{x} \to \tilde{x}_0$) is

$$m \sim m_1\mathscr{R}_1 + \frac{(\tilde{x} - \tilde{x}_0)^2}{2\rho_0} , \tag{2.15}$$

where $m_1\mathscr{R}_1$ is the distance between the static meniscus and the cylinder at $\tilde{x} = \tilde{x}_0$ as shown in figure 4(*a*).

By introducing the change of variables, $\tilde{x} - \tilde{x}_0 = -m_1\xi(3Ca_1\cos\theta_R)^{-1/3}$ and $m = m_1\eta$, the differential equation (2.14) and asymptotic expansion (2.15) become

$$\frac{\mathrm{d}^3\eta}{\mathrm{d}\xi^3} = \frac{\eta - 1}{\eta^3}, \tag{2.16}$$

$$\eta \sim \mathscr{R}_1 + \frac{m_1\xi^2}{2\rho_0(3Ca_1\cos\theta_R)^{2/3}} . \tag{2.17}$$

The differential equation (2.16) is integrated numerically from its asymptotic expansion as $\eta \to 1$ ($m \to m_1$),

$$\eta \sim 1 + \mathscr{A}e^{\xi} + \mathscr{B}e^{-\xi/2}\sin\frac{\sqrt{3}}{2}\xi + \mathscr{C}e^{-\xi/2}\cos\frac{\sqrt{3}}{2}\xi + \cdots, \tag{2.18}$$

to its asymptotic expansion as $\eta \to \infty$ ($m \gg m_1$),

$$\eta \sim \tfrac{1}{2}\mathscr{P}\xi^2 + \mathscr{Q}\xi + \mathscr{R} + \cdots . \tag{2.19}$$

Since we have a third-order differential equation, three of the six constants must be specified; the remaining three are dependent upon the specified constants and determined as part of the numerical solution of the differential equation. Matching the asymptotic expansions in (2.17) and (2.19) specifies one of the constants, $\mathscr{Q} = 0$. It also gives $\mathscr{R}_1 = \mathscr{R}$ and the thickness of the thin film,

$$m_1 \sim \frac{b(x_R)}{2}\mathscr{P}(3Ca_1\cos\theta_R)^{2/3} . \tag{2.20}$$

Here we have used $\rho_0 = b(x_R)/2$.

The asymptotic expansion given in (2.18) must asymptote to a constant film thickness $\eta \to 1$ ($m \to m_1$) as $\tilde{x} \to \infty$; this means that exponentially growing terms must be eliminated. There are two cases to consider: $Ca_1 > 0$ and $Ca_1 < 0$. For $Ca_1 > 0$, $\tilde{x} \to \infty$ corresponds to $\xi \to -\infty$; thus, $\eta \to 1$ implies that $\mathscr{B} = \mathscr{C} = 0$. Having determined three of the constants, $\mathscr{Q}$, $\mathscr{B}$, and $\mathscr{C}$, the remaining three constants are determined by numerically integrating (2.16). The values of the constants that appear in the interface conditions are $\mathscr{P} = 0.6430$ and $\mathscr{R} = 2.8996$.

For $Ca_1 < 0$, $\tilde{x} \to \infty$ corresponds to $\xi \to \infty$; thus, $\eta \to 1$ in (2.18) implies that $\mathscr{A} = 0$ and only two constants have been specified. The missing constant is determined by observing that when $U_1 < 0$ a thin film of thickness m_1 is being pushed into the viscous fluid (see figure 4*a*). This means that the value of m_1 is already known; its value was determined when the thin film was pulled out of the viscous fluid at the other meniscus located at $x = x_L(y,t)$. This implies that (2.20) is an equation for m_1 when $Ca_1 > 0$ and an equation for $\mathscr{P}$ when $Ca_1 < 0$. To allow for all possible values of m_1, (2.16) is integrated for arbitrary $\mathscr{P}$; thus, $\mathscr{R}$, $\mathscr{B}$, and $\mathscr{C}$ are functions of $\mathscr{P}$. Figure 5 shows $\mathscr{R} = F(\mathscr{P})$.

As stated in the introduction, it is assumed that changes in film thickness due to levelling occur on a time scale that is much longer than the time it takes the cylinder to complete one revolution. We also note that even though $\mathscr{R}$ can be negative when a thin film is pushed into the fluid region this does mean that the interface overlaps the wall of the cylinder. The equation of the static meniscus or arc of a circle of radius ρ_R is not valid at $\tilde{x} = \tilde{x}_0$; it is replaced by the solution of the ordinary differential equation, which provides a smooth transition from the interface in the static meniscus region to the thin film of constant thickness without overlap.

The leading-order term of the cross-sectional area A_R given in (2.9), which accounts for the fluid above and below the meniscus, is

$$A_R \sim 2\rho_0^2 - \pi\rho_0^2/2 = (4-\pi)b^2(x_R)/8 . \tag{2.21}$$

This quantity is just the area of the rectangle where the meniscus is located minus the area of the semicircular region filled with air. The contribution to the volume from this term is $O(\delta)$ smaller than the contribution from the first term in (2.9); higher-order terms are neglected.

Before determining the steady state solution for the coating flow problem shown

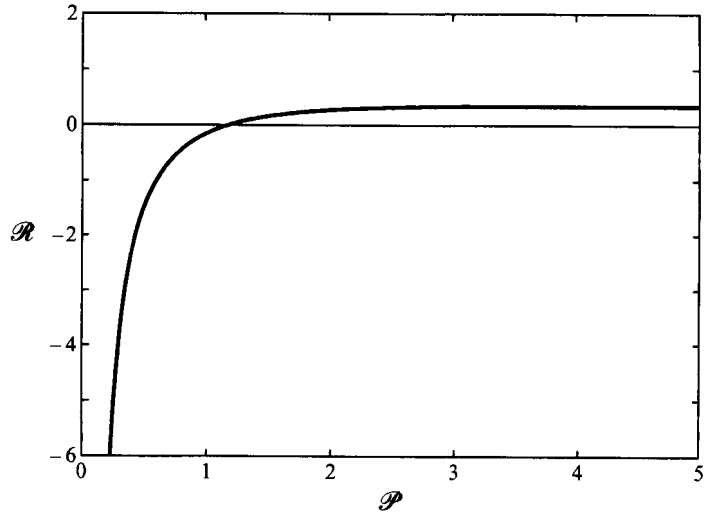

FIGURE 5. $\mathscr{R}$ versus $\mathscr{P}$. Coefficients used to determine the shape of the static meniscus when a thin film is pushed into the viscous fluid region.

in figure 1, we rescale and summarize the boundary conditions. Let $x = a_0\hat{x}$ and $y = a_0\hat{y}$ where a_0 is given in (2.2); thus, $b(\hat{x}) = 1 + \hat{x}^2$ and the lateral curvature $C_j = \hat{C}_j/a_0$. Each thin film has the same thickness at $\hat{x} = \hat{x}_L$ and $\hat{x}_R$. Introducing the dimensionless film thickness $\hat{m}_{ij} = m_i/b(x_j)$, we have

$$m_i = b_0(1 + \hat{x}_L^2)\hat{m}_{iL} = b_0(1 + \hat{x}_R^2)\hat{m}_{iR}\ , \tag{2.22}$$

$$\hat{m}_{ij} = \tfrac{1}{2}\mathscr{P}_{ij}(3Ca_i\cos\theta_j)^{2/3}. \tag{2.23}$$

Here, $i = 1, 2$ and $j = L, R$ refer to the larger and smaller cylinder and left and right meniscus respectively. The kinematic condition given in (2.7) becomes

$$\bar{u}_j\cos\theta_j + \bar{v}_j\sin\theta_j = \frac{T}{\mu}\left[\hat{m}_{1j}Ca_1 + \hat{m}_{2j}Ca_2 + \frac{\partial\hat{x}_j}{\partial\hat{t}}(1 - \hat{m}_{1j} - \hat{m}_{2j})\right]\cos\theta_j\ . \tag{2.24}$$

Here, we have set $t = (\mu a_0/T)\hat{t}$. Perhaps it would be more appropriate to set $t = (a_0/U)\hat{t}$, where U is one of the cylinder velocities or the average of the two velocities. We have used the alternative scaling to give us the freedom to set one or both of the velocities to zero; it also makes the notation simpler when either of the cylinders moves in the opposite direction.

Using (2.13), the pressure jump condition in (2.11) becomes

$$p_0 - p(\hat{x}_j) = \Delta p_j = \frac{T}{b_0}\left[\frac{2}{1 + \hat{x}_j^2}\left(1 \pm \delta\hat{x}_j\cos\theta_j + \hat{m}_{1j}\mathscr{R}_{1j} + \hat{m}_{2j}\mathscr{R}_{2j}\right) \mp \frac{\pi}{4}\delta\hat{C}_j\right]\ . \tag{2.25}$$

In the places where there is a multiple sign, the top and bottom signs correspond to the left and right interface edges respectively. This variation in sign is due to the fact that the menisci at the left and right interface edges open in opposite directions. If we set $V_0 = (y_2 - y_1)A_0$ in the volume equation given in (2.9) and $A_0 = a_0b_0\hat{A}_0$, then $\hat{A}_0$ is the dimensionless area initially occupied by the fluid in the (x, z)-plane; this new parameter must be specified.

3. Steady state solutions

In this section, steady state solutions with straight interface edges are determined; this means that $\hat{x}_L$ and $\hat{x}_R$ are independent of $\hat{y}$ and $\hat{t}$ and that θ_j and $\hat{C}_j$ are both equal to zero. The averaged velocity components are

$$\bar{u} = \frac{Q}{b(x)} = \frac{T}{\mu}\frac{\hat{Q}}{1+\hat{x}^2}, \qquad \bar{v} = 0\,, \tag{3.1}$$

where $\bar{u}$ follows from (2.6) and Q is a constant flow rate. For the reasons discussed above, we have set $Q = b_0 T\hat{Q}/\mu$ instead of scaling Q by b_0 and a characteristic velocity related to the cylinder velocities. In terms of $\hat{Q}$, the kinematic condition (2.24) reduces to

$$\hat{Q} = (1+\hat{x}_j^2)(\hat{m}_{1j}Ca_1 + \hat{m}_{2j}Ca_2)\,. \tag{3.2}$$

Substituting (3.1) into (2.5), we integrate with respect to $\hat{x}$ to get

$$p_0 - p(\hat{x}) = \frac{Ta_0}{b_0^2}\left[-3(Ca_1+Ca_2)g_1(\hat{x}) + \tfrac{9}{2}\hat{Q}g_2(\hat{x}) + \hat{B}\right]\,, \tag{3.3}$$

where

$$g_1 = \tan^{-1}\hat{x} + \frac{\hat{x}}{1+\hat{x}^2}, \qquad g_2 = g_1 + \frac{2\hat{x}}{3(1+\hat{x}^2)^2} \tag{3.4}$$

and $\hat{B}$ is a constant that needs to be determined.

By evaluating (3.3) at $\hat{x}_j$ and substituting into (2.25), we get a jump condition at each meniscus ($j = L, R$). Eliminating $\hat{B}$ from these two equations gives us a single pressure condition. This pressure condition combined with the conservation of fluid condition given in (2.9) provides the two equations that determine $\hat{x}_L$ and $\hat{x}_R$. All other quantities that appear in these equations are determined from equations that are given in §2.4, except for $\hat{Q}$ which is given in (3.2).

4. Linear stability analysis

To analyse the stability of the straight interface edge solutions, we perturb each interface edge with a sinusoidal wave and linearize the equations. Solving these equations determines whether the amplitude of the disturbance is growing or decaying. The perturbations are given by

$$\hat{x}_L = \hat{x}_L^0 + \epsilon_L(\hat{t})\sin k\hat{y},$$

$$\hat{x}_R = \hat{x}_R^0 + \epsilon_R(\hat{t})\sin k\hat{y}\,,$$

where $\epsilon_j = \hat{\epsilon}_j \exp(\sigma\hat{t})$ with $\hat{\epsilon}_L, \hat{\epsilon}_R \ll 1$. Since the linearized equations are coupled, it is important to examine the relative magnitudes of $\hat{\epsilon}_L$ and $\hat{\epsilon}_R$ when $\sigma > 0$ to identify where the disturbance to the interface is more pronounced. In this analysis, it is not possible to perturb the interfaces independently; the form of the perturbation on one interface determines the form of the perturbation in the fluid and on the other interface.

In the fluid, the pressure and velocity components are

$$p = \frac{Ta_0}{b_0^2}[p^0(\hat{x}) + p^1(\hat{x},\hat{t})\sin k\hat{y}],$$

$$\bar{u} = \frac{T}{\mu}[u^0(\hat{x}) + u^1(\hat{x},\hat{t})\sin k\hat{y}], \qquad \bar{v} = \frac{T}{\mu}[v^1(\hat{x},\hat{t})\cos k\hat{y}]\,,$$

where $p^0(\hat{x})$ and $u^0(\hat{x})$ are given in (3.3) and (3.1) respectively and $\hat{t} = (T/a\mu)t$. Using the averaged equations given in (2.5) and (2.6), we get

$$u^1 = -\frac{(1+\hat{x}^2)^2}{12}\frac{\partial p^1}{\partial \hat{x}}, \qquad v^1 = -\frac{(1+\hat{x}^2)^2}{12}kp^1$$

and

$$\frac{\partial^2 p^1}{\partial \hat{x}^2} + \frac{6\hat{x}}{1+\hat{x}^2}\frac{\partial p^1}{\partial \hat{x}} - k^2 p^1 = 0\,. \tag{4.1}$$

Linear independent solutions of the differential equation are determined by numerical integration. For convenience, we set $p^1 = \eta_L(\hat{t})q_L(k,\hat{x}) + \eta_R(\hat{t})q_R(k,\hat{x})$ and choose linear independent solutions that satisfy $q_L(k,\hat{x}_R^0) = 0$ and $q_R(k,\hat{x}_L^0) = 0$.

The above expressions are now substituted into the interface edge conditions and linearized. For simplicity, the equations are only given for $Ca = Ca_1 = Ca_2 \geqslant 0$. The pressure condition (2.25) leads to

$$\eta_j q_j(k,\hat{x}_j^0) = \frac{-12Ca(1-2\hat{m}_j^0)}{[1+(\hat{x}_j^0)^2]^2}\epsilon_j + \frac{4\delta\hat{x}_j^0}{[1+(\hat{x}_j^0)^2]^2}[1 \pm \delta\hat{x}_j^0 + 2\hat{m}_j^0\mathscr{R}_j^0]\epsilon_j$$
$$-\frac{2\delta}{1+(\hat{x}_j^0)^2}[\pm\delta\epsilon_j + 2\hat{m}_j^1\mathscr{R}_j^0 + 2\hat{m}_j^0\mathscr{R}_j^1] \mp \frac{\pi}{4}\delta^2k^2\epsilon_j\,, \tag{4.2}$$

where $j = L$ and R, multiple signs correspond to the left and right interface edges and we have dropped the dependence on i because $Ca_1 = Ca_2$. The first term on the right-hand side results from linearizing $p^0(\hat{x})$ about $\hat{x}_j^0$; the last term accounts for lateral curvature. We further note that since $Ca > 0$, we have $\mathscr{P}_R = 0.6430$ and $\mathscr{R}_R = 2.8996$; thus, $\mathscr{P}_R^1$ and $\mathscr{R}_R^1$ are both equal to zero. In addition, $\hat{m}_R^1$ is also zero, because $\cos\theta_j = 1 + O(\epsilon_j^2)$ in equation (2.23). At the left interface edge, $\hat{m}_L$, $\mathscr{P}_L$, and $\mathscr{R}_L$ are given by $\hat{m}_L = \hat{m}_L^0 + \hat{m}_L^1 \sin k\hat{y}$, etc. Linearizing (2.22) gives

$$\hat{m}_L^1 = \frac{2[\hat{m}_R^0\hat{x}_R^0\epsilon_R - \hat{m}_L^0\hat{x}_L^0\epsilon_L]}{1+(\hat{x}_L^0)^2}. \tag{4.3}$$

We get an identical expression for $\mathscr{P}_L^1$; $\mathscr{R}_L^1$ is determined numerically by linearizing the functional dependence of $\mathscr{R}_L$ on $\mathscr{P}_L$ as shown in figure 5.

Linearizing the kinematic condition given in (2.24), we get

$$[1-2\hat{m}_j^0]\frac{d\epsilon_j}{d\hat{t}} = -\frac{4\hat{x}_j^0\hat{m}_j^0 Ca}{1+(\hat{x}_j^0)^2}\epsilon_j - \frac{[1+(\hat{x}_j^0)^2]^2}{12}[\eta_L\dot{q}_L(k,\hat{x}_j^0) + \eta_R\dot{q}_R(k,\hat{x}_j^0)] - 2Ca\hat{m}_j^1\,, \tag{4.4}$$

where $j = L$ and R. The first term on the right-hand side results from linearizing $u^0(\hat{x})$ about $\hat{x}_j^0$; the second term comes from $u^1(\hat{x})$, where $\dot{q}$ denotes the derivative of q with respect to $\hat{x}$. The volume equation given in (2.9) is also linearized. Since the solution is periodic in $\hat{y}$ and $\sin k\hat{y}$ integrates to zero over a period, the linearized volume equation is satisfied automatically.

Substituting η_L and η_R given in (4.2) into (4.4) gives two coupled equations for ϵ_L and ϵ_R. Setting $\epsilon_j = \hat{\epsilon}_j \exp(\sigma\hat{t})$ and assuming that $\hat{\epsilon}_L$ and $\hat{\epsilon}_R$ are not both zero leads to a quadratic equation for σ. The two roots of the equation are real. For each σ, the relative magnitudes of $\hat{\epsilon}_L$ and $\hat{\epsilon}_R$ are determined.

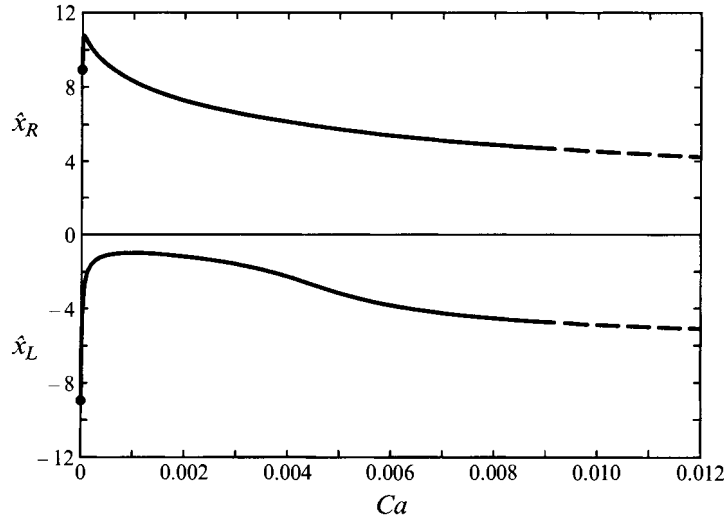

FIGURE 6. Positions of the left and right interface edges as a function of the capillary number $Ca = Ca_1 = Ca_2$. The parameters are $R_2/R_1 = 33/50$, $b_0/R_2 = 1 \times 10^{-4}$, and $\hat{A}_0 = 500$. The right interface becomes unstable at the capillary number where the curves change from solid to dashed lines.

5. Results

5.1. *Primary instability*

The primary instability occurs when the volume of fluid between the cylinders is large enough so that an interface edge does not pass through the region where the gap width is a minimum. Figure 6 shows the position of the left and right interface for $b_0/R_2 = 1 \times 10^{-4}$, $\hat{A}_0 = 500$, and $Ca = Ca_1 = Ca_2 \geqslant 0$. The initial positions ($Ca = 0$) of the interface edges are symmetric about $\hat{x} = 0$ as expected. Note the dramatic change in the position of the interface edges for small capillary number. In particular, $\hat{x}_R$ initially increases due to the motion of the cylinders and then decreases as more fluid moves into the thin films; this has been observed in experiments. The position of $\hat{x}_L$ moves towards $\hat{x} = 0$ and will pass to the other side ($\hat{x}_L > 0$) if $\hat{A}_0$ is small enough; otherwise, it will begin to move away from $\hat{x} = 0$ until the right interface becomes unstable.

For co-rotating cylinders, $Ca_1 \geqslant 0$ and $Ca_2 \geqslant 0$, the critical capillary numbers where the right interface becomes unstable are very insensitive to the amount of fluid present as long as $\hat{A}_0$ is not too close to the threshold value that separates solutions with a primary instability from those with an inverse instability. As $\hat{A}_0$ increases, the change in the position of the right interface at the critical capillary number is very small; the position of the left interface decreases to accommodate the increased volume of fluid. This means that for a sufficient amount of fluid and co-rotating cylinders, the assumption made in the past that the left interface is far enough away from the right interface that it can be ignored in the analysis is valid.

To illustrate the effect of $\hat{A}_0$ on the solution, we have plotted the decay rate σ as a function of the wavenumber k at the critical capillary number (see figure 7). The second root of the quadratic equation for σ is always negative and has not been plotted. Observe that $\sigma = 0$ at $k = 0$. This result was proven analytically and is true for both co-rotating and counter-rotating cylinders and is not dependent upon the perturbation results; thus, it is true for arbitrary Ca_1 and Ca_2. To show this result, we

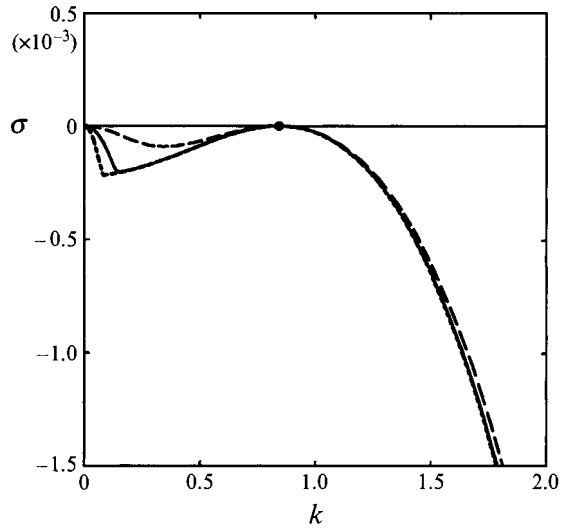

FIGURE 7. —, Decay rate σ versus wavenumber k at the critical capillary number for the parameters given in figure 6 ($\hat{A}_0 = 500$). The other curves show the effect of changing the amount of fluid between the cylinders: – – –, $\hat{A}_0 = 450$ and - - -, $\hat{A}_0 = 1000$. Dimensionless decay rate shown is very small due to the choice of scaling for t.

first note that at $k = 0$ linearly independent solutions of (4.1) are $g_2(\hat{x})$ given in (3.4) and 1. Setting $q_L = g_2(\hat{x}) - g_2(\hat{x}_R)$ and $q_R = g_2(\hat{x}) - g_2(\hat{x}_L)$, we get that both $\dot{q}_L(\hat{x}_j^0)$ and $\dot{q}_R(\hat{x}_j^0)$ are equal to $(8/3)[1 + (\hat{x}_j^0)^2]^{-3}$. This result and the result for $\hat{m}_L^1$ given in (4.3) are now substituted into (4.4). We now multiply both sides of the equation by $[1 + (\hat{x}_j^0)^2]$ and find that the right-hand sides of the two equations ($j = L, R$) are identical. This means that the constant term in the quadratic equation for σ at $k = 0$ is missing and one of the two roots must be zero.

In figure 7, the curves corresponding to $\hat{A}_0 = 500$ and $\hat{A}_0 = 1000$ are nearly identical except at small values of k. The critical capillary number and wavenumber are $Ca = 8.93 \times 10^{-3}$ and $k = 0.847$ for $\hat{A}_0 = 500$ and $Ca = 8.94 \times 10^{-3}$ and $k = 0.846$ for $\hat{A}_0 = 1000$. The bend in these curves is caused by an imperfect bifurcation. The graph of the second root of the quadratic equation (not shown) begins at $(k, \sigma) = (0, -0.22 \times 10^{-3})$ goes towards the bend in the curve shown and then bends downward just before it reaches this curve. The small parameter $1/\hat{A}_0$ that is needed when we account for the left interface leads to a dramatic change in the bifurcation diagram from two crossing curves ($\hat{A}_0 \to \infty$) to the situation described above.

To show the effect of $\hat{A}_0$ on the solution as we approach the threshold value that separates the primary and inverse stabilities, we have plotted the curve corresponding to $\hat{A}_0 = 450$. At this value of $\hat{A}_0$, we get $Ca = 8.77 \times 10^{-3}$ and $k = 0.843$. The shape of the curve between $k = 0$ and the critical wavenumber is flattening out and approaching the k-axis. At $\hat{A}_0 = 400$, the difference between this part of the curve and the k-axis would not be visible on this plot. At $\hat{A}_0 = 400$, we get $Ca = 8.14 \times 10^{-3}$ and $k = 0.442$. Note that the critical wavenumber is moving towards $k = 0$ and that the second derivative would be nearly zero at the origin. At $\hat{A}_0 = 350$, the left interface passes through the minimum gap region and there is no longer a primary instability.

For $\hat{A}_0 \geqslant 500$, the ratio of $\hat{\epsilon}_R$ to $\hat{\epsilon}_L$ is greater than 15 to 1; thus, the right interface is identified as the unstable interface. At $\hat{A}_0 = 450$, the ratio is about 3 to 2 so that the disturbances are nearly equal in magnitude.

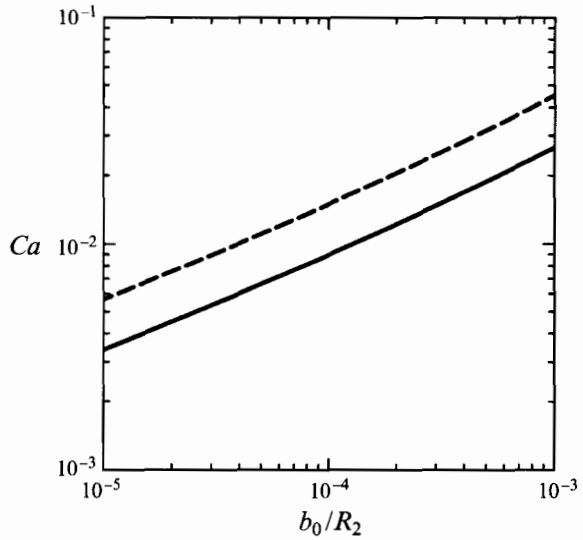

FIGURE 8. Capillary number versus b_0/R_2 for the primary instability. —, Co-rotating cylinders with $Ca = Ca_1 = Ca_2$. – – –, One of the cylinders is stationary; thus, $Ca = Ca_1$ or $Ca = Ca_2$.

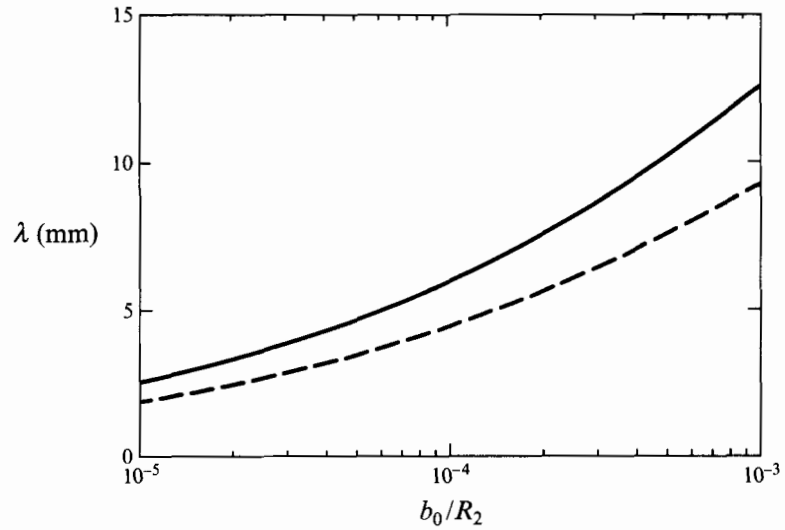

FIGURE 9. Critical wavelength versus b_0/R_2 for the primary instability where $R_2 = 33$ mm. —, Co-rotating cylinders with $Ca = Ca_1 = Ca_2$. – – –, One of the cylinders is stationary ($Ca = Ca_1$ or $Ca = Ca_2$).

Figure 8 shows the critical capillary number when the amount of fluid is considerably larger than the threshold value and $b_0/R_2 \leqslant 10^{-3}$. We have not done the calculations at larger values of b_0/R_2 because the corresponding critical capillary numbers would be too large for the perturbation results of the interface conditions to be valid. Figure 9 shows the critical wavelength λ in physical units when $R_2 = 33$ mm. The dimensionless wavelength $\hat{\lambda}$ is a decreasing function of b_0/R_2; figure 9 has been plotted using physical units to avoid creating the false impression that λ is also a decreasing function of b_0/R_2.

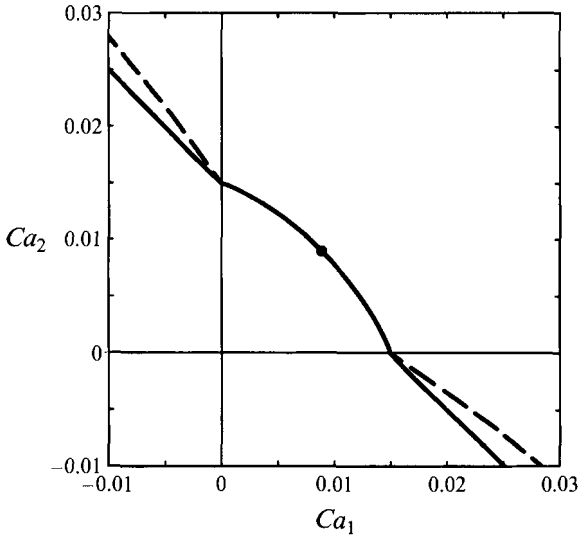

FIGURE 10. Critical capillary numbers for the primary instability when the cylinders rotate independently. The parameters are $R_2/R_1 = 33/50$ and $b_0/R_2 = 1 \times 10^{-4}$; —, $\hat{A}_0 = 500$ and - - -, $\hat{A}_0 = 1000$. The point on the curve corresponds to the critical capillary number shown in figure 6.

Figure 10 shows the critical capillary numbers for $b_0/R_2 = 1 \times 10^{-4}$ and $\hat{A}_0 = 500$ and 1000. This graph shows that the co-rotating problem is insensitive to changes in $\hat{A}_0$. It also shows that the counter-rotating problem does depend on fluid volume. This is to be expected since in the counter-rotating problem, one of the thin films is now pulled out of the viscous fluid at the left interface and pushed back into the viscous fluid at the right interface. The thickness of this film depends on the position of the left interface; thus, it is no longer possible to decrease the position of the left interface to accommodate additional volume without affecting the solution at the right interface.

Notice that the curve shown in figure 10 has the same qualitative shape as the experimental results shown in figure 2 (especially for $\hat{A}_0 = 500$). A direct comparison between the results cannot be made because the gap width in figure 2 is $b_0/R_2 = 7.55 \times 10^{-3}$. This gap width leads to capillary numbers that are too large for the perturbation results to be valid.

5.2. *Inverse instability*

The inverse instability occurs when the volume of fluid between the cylinders is small enough that an interface edge passes through the region where the gap width is a minimum. We begin by examining the special case $Ca = Ca_1 = Ca_2$ in detail. Figure 11 shows the position of the left and right interfaces for $b_0/R_2 = 1 \times 10^{-4}$ and $\hat{A}_0 = 40$. As the capillary number increases, the thin films become thicker. Since the total amount of fluid is conserved, the amount of fluid between the tips of the menisci decreases and the tips move towards each other. As Ca is increased further, the position of the left interface becomes positive. At $Ca = 2.209 \times 10^{-3}$, there is a turning point leading to an upper branch of steady state solutions with straight edges. We note that on the upper branch the tips of the menisci are moving towards each other even though the capillary number is decreasing. This is possible because

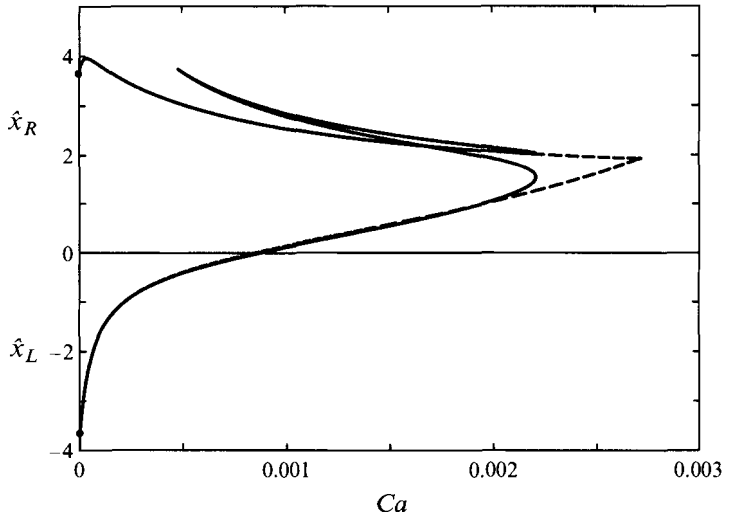

FIGURE 11. —, Positions of the left and right interface edges as a function of the capillary number $Ca = Ca_1 = Ca_2$. The parameters are $R_2/R_1 = 33/50$, $b_0/R_2 = 1 \times 10^{-4}$, and $\hat{A}_0 = 40$. The left interface passes through the minimum gap width at $\hat{x} = 0$. There is a turning point at $Ca = 2.209 \times 10^{-3}$. – – –, Positions of the interface edges based upon a simplified pressure jump condition. There is no longer a turning point. For both sets of curves $\hat{x}_L$ and $\hat{x}_R$ are equal when all the fluid is located in the thin films.

thicker thin films can be achieved by increasing Ca or by increasing $\hat{x}_R$ (see (2.20) or (2.22)). On the upper branch of solutions, $\hat{x}_R$ is increasing as Ca decreases.

Regardless of their stability, there are no steady state solutions with straight edges past the turning point. This result is very different from the primary instability problem where steady state solutions exist for large capillary number. We note that our solutions are only valid as long as the separation between the tips of the menisci $\Delta x = x_R - x_L$ is $O(a_0)$ and not $O(b_0)$ or equivalently $\hat{x}_R - \hat{x}_L \gg \delta$. At the turning point in figure 11, $\hat{x}_R - \hat{x}_L = 0.497$ and $\delta = 0.00412$, so this condition is certainly satisfied.

Table 1 gives the capillary number and the positions of the interface edges at the turning point for different values of b_0/R_2 and $\hat{A}_0$. Figure 12 is a plot of the capillary numbers at the turning points that are given in table 1. It is clear from the plot that turning point capillary number increases when either b_0/R_2 or $\hat{A}_0$ increases. Recall that the physical area where the fluid is located is $A_0 = a_0 b_0 \hat{A}_0$; thus, increasing b_0/R_2 or $\hat{A}_0$ increases the total volume of fluid.

To illustrate the importance of the small terms in the pressure jump condition, we neglect all terms in (2.25) except for the leading-order term of $O(T/b_0)$. The dashed curves in figure 11 give the positions of the interface edges for this case. The simpler pressure jump condition gives good results until the turning point is approached. The new solution does not have a turning point. We denote the capillary number where the dashed curves meet as the maximum capillary number Ca_m.

To approximate the functional relationship between b_0/R_2, $\hat{A}_0$, and the capillary number at the turning point, we determine an asymptotic relationship between b_0/R_2, $\hat{A}_0$, and Ca_m. To derive this asymptotic formula, we use the simpler pressure condition and neglect $\hat{Q} = O(Ca^{5/3})$ in (3.3) in comparison with the $O(Ca)$ term. This leads to

$\hat{A}_0$	$b_0/R_2 = 10^{-5}$	$b_0/R_2 = 10^{-4}$	$b_0/R_2 = 10^{-3}$
10	2.803×10^{-4}	1.078×10^{-3}	3.998×10^{-3}
	0.656	0.790	0.885
	0.809	1.041	1.280
20	4.328×10^{-4}	1.589×10^{-3}	5.792×10^{-3}
	0.996	1.132	1.203
	1.215	1.487	1.763
40	6.145×10^{-4}	2.209×10^{-3}	8.063×10^{-3}
	1.400	1.536	1.564
	1.706	2.033	2.357
100	9.171×10^{-4}	3.265×10^{-3}	1.220×10^{-2}
	2.066	2.200	2.077
	2.541	2.970	3.363
200	1.212×10^{-3}	4.318×10^{-3}	
	2.705	2.823	
	3.367	3.898	
400	1.585×10^{-3}		
	3.500		
	4.421		
1000	2.240×10^{-3}		
	4.857		
	6.283		

TABLE 1. Values of $Ca_1 = Ca_2$, $\hat{x}_L$ and $\hat{x}_R$ at the turning point for $R_2/R_1 = 33/50$ and different values of b_0/R_2 and fluid volume corresponding to the dimensionless cross-sectional area $\hat{A}_0$. Blank spaces indicate parameter values at which the primary instability occurs.

a single pressure condition, $F(\hat{x}_L) = F(\hat{x}_R)$, where

$$F(\hat{x}) = \frac{2\delta}{1+\hat{x}^2} + 6Ca\left[\tan^{-1}\hat{x} + \frac{\hat{x}}{1+\hat{x}^2}\right]. \tag{5.1}$$

See the discussion at the end of §3 for the derivation of a single pressure equation. $F(\hat{x})$ is an increasing function for $\hat{x} < 3Ca/\delta$ and a decreasing function for $\hat{x} > 3Ca/\delta$; thus, $\hat{x}_L \leqslant 3Ca/\delta$ and $\hat{x}_R \geqslant 3Ca/\delta$. The maximum capillary number occurs when $\hat{x}_L = \hat{x}_R = 3Ca/\delta$ and when all the liquid is in the thin films, $A_0 \sim 2\pi(R_1 + R_2)m$ or

$$\begin{aligned}\hat{A}_0 &\sim \pi\left(\frac{R_2}{b_0}\right)\left(\frac{R_1}{R_2}+1\right)\delta(1+\hat{x}_R^2)\mathscr{P}(3Ca)^{2/3} \\ &\sim 4.36\, Ca^{2/3}\left(\frac{b_0}{R_2}\right)^{-1/2} + 232\, Ca^{8/3}\left(\frac{b_0}{R_2}\right)^{-3/2}.\end{aligned} \tag{5.2}$$

The parameter δ is given below (2.2) and $\mathscr{P} = 0.6430$. The numerical coefficients depend on R_2/R_1; they were evaluated for $R_2/R_1 = 33/50$. This asymptotic relationship is also plotted in figure 12. The dashed lines in the figure end at values where twice the film thickness equals the minimum gap width b_0; otherwise, the thin films

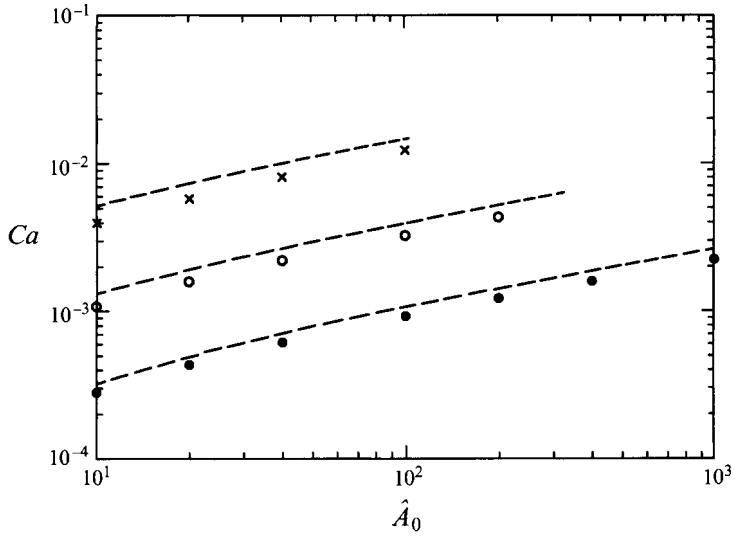

FIGURE 12. Capillary number at the turning point versus $\hat{A}_0$. •, $b_0/R_2 = 10^{-5}$; ○, $b_0/R_2 = 10^{-4}$; ×, $b_0/R_2 = 10^{-3}$. – – –, Asymptotic relationship for the maximum capillary number using simplified pressure jump condition.

collide as they pass through the place where the gap width is a minimum. Since (5.2) is actually an asymptotic relationship for Ca_m and not the turning point capillary number, it is not surprising that the curves are higher than the data points that specify turning point capillary numbers; nonetheless, they do seem to have the same functional form. When $\hat{x}_R^2 = 9Ca^2/\delta^2 \gg 1$, the first term on the right-hand side of (5.2) can be neglected; the resulting equation is expressed as

$$Ca \sim 0.130\, \hat{A}_0^{3/8} \left(\frac{b_0}{R_2}\right)^{9/16}. \tag{5.3}$$

This asymptotic relationship is valid for the right half of the plot in figure 12 where the curves on the log-log plot are nearly straight lines. Using the method of least squares and the functional relationship given in (5.2), a single equation that approximates all of the data for the turning point capillary numbers in table 1 is determined. The new coefficients in (5.2) are 4.70 and 358 which gives 0.110 for the new coefficient in (5.3). Finding the new coefficients in (5.2) is equivalent to scaling $\hat{A}_0$ and Ca; thus, the new coefficients correspond to replacing $\hat{A}_0$ and Ca in (5.2) by $1.05\hat{A}_0$ and $1.20Ca$. This means that Ca_m is approximately 20% larger than the turning point capillary number. On a log-log plot these scalings correspond to translating the curves in figure 12 down and slightly to the left.

Using the linear stability analysis discussed above, the stability of the steady state solutions is determined. One of the roots is negative for all k and Ca; thus, we focus our attention on the other root which we denote as $\sigma(k, \hat{x}_L)$. It is more convenient to use $\hat{x}_L$ instead of Ca as the parameter in the problem because of the presence of the turning point in the steady solutions. Figure 13 shows typical curves for σ versus k at three different values of $\hat{x}_L$; the middle curve corresponds to the critical point.

As before, we observe that $\sigma = 0$ at $k = 0$ for all values of $\hat{x}_L$. The critical point occurs at that value of $\hat{x}_L$ where the graph of σ versus k at $k = 0$ changes from being concave down to concave up or where the second derivative of σ at $k = 0$ vanishes.

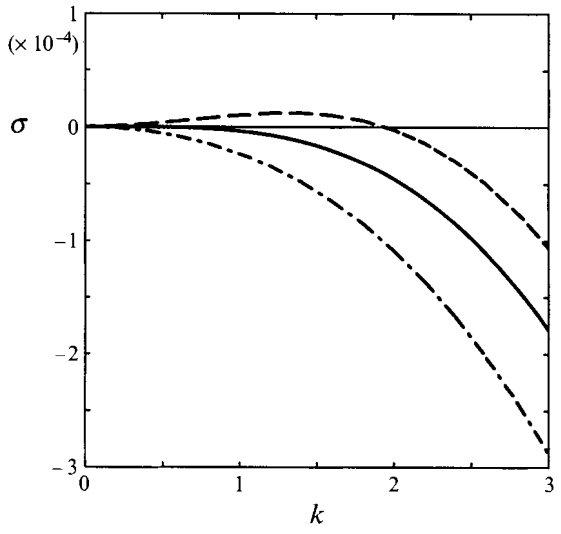

FIGURE 13. Typical set of curves for the decay rate σ versus wavenumber k. The lower and upper curves correspond to steady state solutions that are stable and unstable respectively. On the middle curve, the second derivative of σ with respect to k at $k = 0$ is zero. This curve corresponds to a steady state solution that is neutrally stable. Decay rate is very small due to the choice of scaling for t.

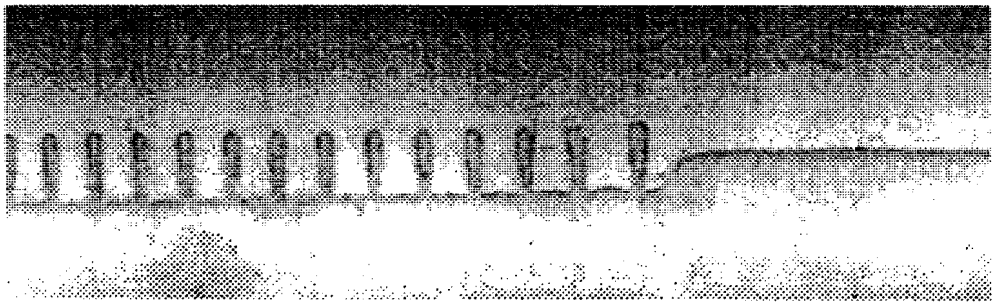

FIGURE 14. The experimental result of Michalland (1992) shows the two steady states for the left interface edge. The front is moving towards the right. Reprinted with permission.

This means that in contrast to the primary instability problem, it is not possible to find a critical wavenumber k from the linear stability analysis.

The relative error between the calculated values for the the capillary number at the turning point and the critical capillary number is on the order of 0.1%; thus, we conclude that they are equal. The lower branch of solutions for $\hat{x}_L$ and $\hat{x}_R$ that starts at $Ca = 0$ is stable and the upper branch of solutions past the turning point is unstable. By examining the relative magnitudes of the amplitudes of the disturbances at the turning point, it is clear that $\hat{x}_L$, the interface that has passed through the minimum gap width, is the unstable interface. In addition, the presence of the turning point means that there should be a jump to a new branch of solutions and not a gradual change to a small-amplitude sinusoidal wave which occurs for the primary instability. This phenomenon has been observed in the experiments of Michalland (1992). Figure 14 shows a photograph in which the straight interface solution is changing to the new steady state solution.

Figure 15 shows the positions of the menisci or interface edges for counter-rotating

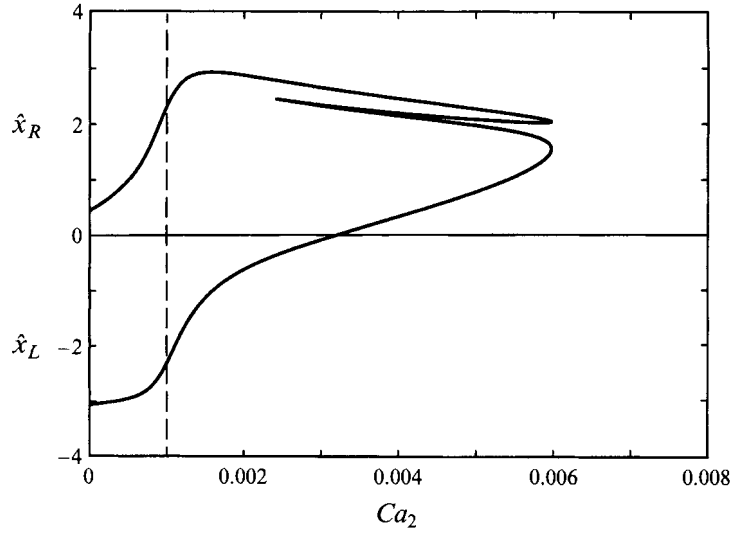

FIGURE 15. —, Positions of left and right interface edges versus Ca_2 for counter-rotating cylinders. Dimensionless parameters are $Ca_1 = -0.001$, $b_0/R_2 = 10^{-4}$, $R_2/R_1 = 33/50$, and $\hat{A}_0 = 40$. The dashed line indicates that the positions of the interfaces about $\hat{x} = 0$ are symmetric when the cylinders are rotating in opposite directions with equal speeds.

cylinders. We have set $Ca_1 = -0.001$ and have increased the other capillary number Ca_2. When $Ca_2 = -Ca_1$, the positions of the interfaces are symmetric about $\hat{x} = 0$ as expected. There is a turning point in the counter-rotating case just like in the co-rotating case. Again, the turning point corresponds to the critical capillary number.

We now let Ca_1 and Ca_2 be independent parameters. Figure 16 shows the values of the two capillary numbers at which turning points occur or equivalently the capillary numbers at which the interface that has passed through the minimum gap width becomes unstable. Since the geometry shown in figure 1 is symmetric about $\hat{x} = 0$, there is a second curve of turning points corresponding to $(-Ca_1, -Ca_2)$ that is not shown. There are similar curves for each of the pairs of parameters given in table 1. The curves are not symmetric about $Ca_1 = Ca_2$ because the amount of viscous fluid that remains between the two interface edges depends on whether a thin film of a given thickness coats the larger cylinder or smaller cylinder.

6. Summary

Coating flow problems that have free surfaces with significant lateral variations along an interface edge can be solved using a fully three-dimensional formulation, but not without very intensive computations. An alternative approach is to approximate the three-dimensional problem by an appropriate two-dimensional problem. In the narrow gap between the cylinders and away from the menisci, the lubrication approximation leads to two-dimensional averaged equations for the velocity and pressure.

In the vicinity of a meniscus, the flow becomes three-dimensional and the averaged equations are no longer valid. Instead of abandoning the two-dimensional approach, we take advantage of the fact that in most coating flow problems variations along the interface edge occur on a length scale that is much larger than the small distance across the gap. This allows us to approximate the flow in the neighbourhood of a

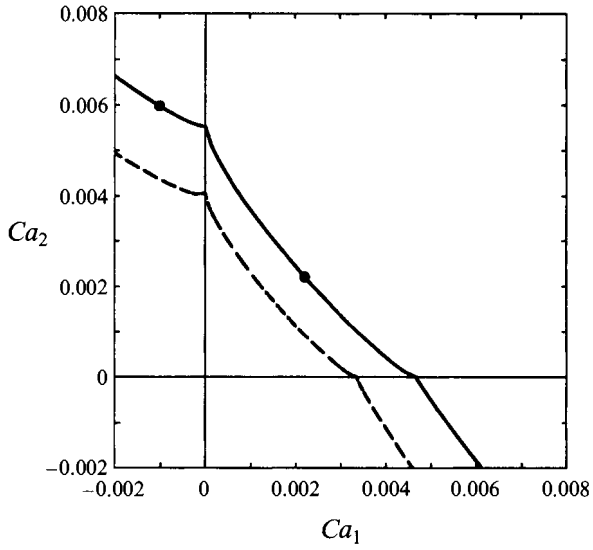

FIGURE 16. Critical capillary numbers for the inverse instability when the cylinders rotate independently. Parameters are $R_2/R_1 = 33/50$ and $b_0/R_2 = 1 \times 10^{-4}$; - - -, $\hat{A}_0 = 20$ and —, $\hat{A}_0 = 40$. The points on the solid curve correspond to the turning points shown in figures 11 and 15.

meniscus by a series of two-dimensional problems in the plane perpendicular to the interface edge.

Solutions of these problems lead to interface conditions that connect solutions of the averaged equations in the viscous fluid region with equations that describe the thin liquid films. For example, each of the F_i in (1.1) is determined from the solution of an appropriate two-dimensional problem in the neighbourhood of the meniscus. Here the F_i have been determined for small capillary numbers using perturbation methods, but they can also be determined for $O(1)$ capillary numbers using numerical methods. Particular attention has been given to accounting for both interfaces and for thin films being pulled out of and pushed into the viscous fluid region.

The two-interface problem allows us to examine phenomena that occur when the cylinders are rotating in opposite directions or when the volume of fluid between the cylinders is small. Without loss of generality, the velocities of the cylinders are restricted to $Ca_1 + Ca_2 \geqslant 0$. With this assumption, the fluid volume determines whether the left interface edge passes through the minimum gap width. If it does not, there is a primary instability; if it does, there is an inverse instability. The characteristics of these instabilities are very different from each other. The right interface becomes unstable for the primary instability and the left interface becomes unstable for the inverse instability. If the left interface edge does not move to the opposite side, there is a single steady state solution with straight interface edges at each value of capillary number. If it does pass to the other side, the steady state solutions exhibit a turning point; there are no solutions with straight interface edges past the turning point.

The primary instability is supercritical; the interface edge changes gradually from being straight to an interface with deep cells. A critical wavenumber at the onset of the instability is determined. The inverse instability is subcritical; there is a dramatic change in the solution from a straight interface to an interface with deep cells. A critical wavenumber cannot be determined from the linear stability analysis. The characteristics described here for each type of instability appear to be general; they

do not depend upon the values of the parameters b_0/R_2, $\hat{A}_0$, or whether the cylinders are co-rotating or counter-rotating. The plots of the critical values of the capillary numbers (see Figures 10 and 16) are also different. When the capillary numbers are both positive, the curve for the primary instability is concave toward the origin and independent of fluid volume; the curve for the inverse instability is concave away from the origin and dependent upon fluid volume.

Though there is qualitative agreement between the theory and experiments, it still needs to be determined whether there is quantitative agreement. To make a quantitative comparison, it is necessary to perform the experiments at smaller values of b_0/R_2 or numerically determine interface conditions that are valid for $O(1)$ capillary numbers. It is also necessary to know the values of $\hat{A}_0$ in the experiments. Only the results for the primary instability with co-rotating cylinders are independent of fluid volume.

The averaged equations and interface conditions discussed here provide a framework for examining interface edges with deep cells. It is also hoped that it will eventually lead to a better understanding of some of the time-dependent phenomena observed in recent experiments.

The author wishes to express his appreciation to G. M. Homsy for many stimulating discussions during a sabbatical leave at Stanford University in 1990–91.

REFERENCES

BRETHERTON, F. P. 1961 The motion of long bubbles in tubes. *J. Fluid Mech.* **10**, 166–188.

COYLE, D. J., MACOSKO, C. W. & SCRIVEN, L. E. 1986 Film-splitting flows in forward roll coating. *J. Fluid Mech.* **171**, 183–207.

COYLE, D. J., MACOSKO, C. W. & SCRIVEN, L. E. 1990 Stability of symmetric film-splitting between counter-rotating cylinders. *J. Fluid Mech.* **216**, 437–458.

HAKIM, V., RABAUD, M., THOMÉ, H. & COUDER, Y. 1990 Directional growth in viscous fingering. In *New Trends in Nonlinear Dynamics and Pattern Forming Phenomena: The Geometry of Nonequilibrium* (ed. P. Coullet & P. Huerre), pp. 327–337. Plenum.

LANDAU, L. & LEVICH, B. 1942 Dragging of a liquid by a moving plate. *Acta Physicochim. URSS* **17**, 42–54.

MICHALLAND, S. 1992 Etude des differents regimes dynamiques de l'instabilite de l'imprimeur. Thesis, L'École Normale Supérieure, Paris, France.

MYSELS, K. J., SHINODA, K. & FRANKEL, S. 1959 *Soap Films: Studies of Their Thinning*. Pergamon.

PAN, L. & BRUYN, J. R. DE 1993 Spatially uniform traveling cellular patterns at a driven interface. *Phys. Rev.* E **49**, 483–493.

PARK, C.-W. & HOMSY, G. M. 1984 Two-phase displacement in Hele-Shaw cells: theory. *J. Fluid Mech.* **139**, 291–308.

PEARSON, J. R. A. 1960 The instability of uniform viscous flow under rollers and spreaders. *J. Fluid Mech.* **7**, 481–500.

PITTS, E. & GREILLER, J. 1961 The flow of thin liquid films between rollers. *J. Fluid Mech.* **11**, 33–50.

RABAUD, M. & HAKIM, V. 1991 Shape of stationary and travelling cells in the printer's instability. In *Instabilities and Nonequilibrium Structures III* (ed. E. Tirapegui & W. Zeller), pp. 217–223. Kluwer Academic.

RABAUD, M., MICHALLAND, S. & COUDER, Y. 1990 Dynamical regimes of directional viscous fingering: spatiotemporal chaos and wave propagation. *Phys. Rev. Lett.* **64**, 184–187.

REINELT, D. A. 1987 Interface conditions for two-phase displacement in Hele-Shaw cells. *J. Fluid Mech.* **183**, 219–234.

RUSCHAK, K. J. 1982 Boundary conditions at a liquid/air interface in lubrication flows. *J. Fluid Mech.* **119**, 107–120.

SAFFMAN, P. G. & TAYLOR, G. I. 1958 The penetration of a fluid into a porous medium or Hele-Shaw cell containing a more viscous liquid. *Proc. R. Soc. Lond.* A **245**, 312–329.

SAVAGE, M. D. 1977 Cavitation in lubrication. Part 1. On boundary conditions and cavity-fluid interfaces. *J. Fluid Mech.* **80**, 743–755.